Hybrid Wall Treatment for RANS in Complex Geometry Turbulent Flows[☆]

M. A. Christon[a]

[a] *Computational Sciences International, Los Alamos, NM 87544, USA*

Abstract

This paper presents a hybrid two-layer wall treatment for RANS calculations on unstructured grids that can be extended to multiple $k-\epsilon$ models without the need to re-tune/re-calibrate model coefficients. The objective of the hybrid wall treatment is to provide a generalized wall treatment that asymptotes to a high-Reynolds number treatment when $y^+ > \sim 30$ while delivering a low-Reynolds number behavior as the laminar sublayer is resolved $y^+ < \sim 5$. As a basis for comparison, the so-called "scalable" wall functions, touted as being y^+-insensitive, are examined with the hybrid two-layer wall treatment in the context of variable mesh resolution for a $Re_\tau = 590$ turbulent channel flow. Two different mesh refinement strategies are used to test the sensitivity of each formulation to the near-wall mesh resolution as the boundary layer is resolved. Next, the behavior of the hybrid wall treatment is extended to turbulent flow past a surface-mounted cube where there is massive separation, adverse pressure gradients, and multiple three-dimensional recirculation points. The scalable wall functions, while robust, are really still only viable for the high-Reynolds number limit and do not converge to the correct physical boundary layer solution under mesh refinement. In contrast, the hybrid wall treatment, although not perfect, does provide the doubly-asymptotic behavior with both high-Reynolds number behavior for coarse meshes, and the low-Reynolds number behavior when the boundary layer is resolved. Application to the mounted cube problem has proven the hybrid wall treatment to be incredibly robust even in the face of three-dimensional flows with massive separation. The hybrid wall treatment, because it is simple to implement, computationally efficient, and easily extensible to $k-\epsilon$ variants without re-calibration, provides a a good alternative to low-Re approaches.

Keywords: incompressible flow, projection method, turbulent flow, hybrid wall treatment, wall functions, separated flow

[☆] Computational Sciences Internationa, Report CSI-2017-1

Email address: machriston@c-sciences.com (M. A. Christon)

URL: http://www.c-sciences.com (M. A. Christon)

1. Introduction

Wall functions, sometimes referred to as "numerical graffiti" in the CFD community, were introduced in the 1970's as a mechanism to bridge the gap between high-Reynolds number $k-\epsilon$ models and no-slip/no-penetration walls. The high-Reynolds number (HRN) approach requires that the first mesh point from a no-slip/no-penetration wall, where degrees-of-freedom are located, be placed in the fully-turbulent region of the flow ($y^+ > \sim 30$). In contrast, the use of low-Reynolds number (LRN) models require the first mesh point to be placed in the laminar sublayer ($y^+ < \sim 10$). In complex geometry flows, precisely controlling the mesh spacing to maintain the y^+ requirements for either the HRN or the LRN approach can prove problematic.

In contrast to the HRN and LRN methods, hybrid or compound wall treatments are designed to be doubly asymptotic by delivering a wall-function behavior on coarse meshes ($y^+ > \sim 30$), a low-Reynolds number behavior for $y^+ < \sim 5$, and reasonable results in the buffer region in between. Motivated by recent work on compound wall treatments, e.g., [1, 2, 3], this work develops a hybrid two-layer approach that is easily implemented and extensible to multiple $k-\epsilon$ models without resorting to re-tuning/re-calibrating model coefficients. In this work, the standard and RNG models are used as prototypical $k-\epsilon$ models. As a basis for comparison, the Spalart-Allmaras (LRN) model and the so-called "scalable" wall functions for the $k-\epsilon$ models are compared with the hybrid two-layer wall treatment.

Before proceeding with the formulation, a brief review of work in the area of wall treatment for RANS computations is presented. Bredberg [4] presents a comprehensive study of wall functions and both LRN and HRN approaches. Similarly, Albets-Chico, et al., [5] present a detailed analysis of wall function approaches, while Durbin [6] reviews the use of limiters and various wall treatments. As pointed out by Durbin [6]: "*The holy grail is a grid-independent formulation*".

The underpinnings for many of the HRN wall treatments used in CFD codes today derive from the 1974 paper by Launder and Spalding [7]. This type of wall modeling was designed for use with meshes where the first near-wall mesh point is placed in the fully-turbulent logarithmic region of the boundary layer. From a practical point of view, ensuring that all the near wall cells are outside the viscous sublayer for complex flow geometries is problematic and will likely not produce accurate wall shear and heat flux. In addition, the precise location of the logarithmic region is solution dependent and may vary during the solution process.

In contrast, low-Reynolds number models permit solving the $k-\epsilon$ equations through the laminar sublayer. In 1984, Patel, et al. [8] provided an in-depth analysis of eight competing low-Reynolds number $k-\epsilon$ closures and found all to be lacking on physical grounds. Although used, the numerical stiffness associated with the ϵ equation in the laminar sublayer has limited the widespread adoption of the these LRN models in the CFD community. Goldberg, et al. [9] made use of a realizable time-scale and a damping function for the turbulent

eddy-viscosity in order to develop a $k-\epsilon$ model that could be integrated to the wall using an asymptotic dissipation rate for the wall boundary condition. In order to obtain a low-Reynolds number $k-\epsilon$ model, Rahman and Siikonen [10] proposed a series of modifications to the standard $k-\epsilon$ model that include a wall damping function for the eddy viscosity, a realizable time-scale, and variable model coefficients C_{ϵ_1} and C_{ϵ_2}. For this work, attempting to extend the approach of Rahman-Siikonen to the RNG $k-\epsilon$ model has proven problematic because significant re-calibration of the model coefficients is required.

In 1988, Chen and Patel [11] introduced a two-layer model that integrates the one-equation model (turbulent kinetic energy) of Wolfshtein [12] to the wall, and represents the near-wall dissipation rate in terms of the turbulent kinetic energy and a dissipation length scale. In the fully-turbulent region of the flow-domain, the two-equation $k-\epsilon$ model is solved. Limited to structured meshes and simple geometries, the Chen and Patel model used grid lines to segregate the domain into a fully-turbulent region and near-wall region. In contrast, Grotjans and Menter [13] formulated a y^+-insensitive wall function that relies on a shift in the velocity profile in the wall-normal direction. Initially implemented in the CFX code, this resulted in the so-called "scalable" wall function approach found in some commercial codes.

Craft, et al. [14, 15] report on the development of an analytic representation of the dynamic variables necessary for a wall closure. The approach relies on a proposed representation of the turbulent viscosity, molecular viscosity and turbulent dissipation rate in wall-attached cells. This approach permits inclusion of temperature dependent fluid properties, albeit with complex functions required for the implementation. Shih, et al. [16] proposed a generalized approach to wall functions using a piecewise polynomial representation of the variation of velocity. In a similar vein, Utyuzhnikov [17] used analytical functions with a linear model equation for the near-wall behavior in order to develop wall functions. The work by Bazilevs, et al. [18] uses a modified weak boundary condition with a stabilized finite element formulation that incorporate the law-of-the-wall permitting relatively coarse boundary layer meshes to be used. Alternatively, a novel approach to wall treatment based on enriching the polynomial function space with the law-of-the-wall was used by Krank and Wall [19].

Knopp, et al. [20] consider the use of a hybrid wall treatment to permit grid adaptation in the near-wall region while permitting application to non-equilibrium flows. A compound wall treatment for the $\zeta-f$ model [21] was developed by Popovac and Hanjalic [1] to relax the strict y^+ requirements for the LRN and HRN methodologies. Here, the blending functions of Kader [22] were used for the velocity, and wall shear stress. Rahman and Siikonen [2] use a similar approach, but with a highly-modified $k-\epsilon$ model that also relaxes y^+ requirements. Saric, et al. [3] present a similar hybrid wall treatment with an emphasis on achieving accurate wall heat transfer.

In the following sections, the formulation for the "scalable" wall function and for a hybrid two-layer model are presented. The behavior of both approaches under mesh refinement is explored in the context of a $Re_\tau = 590$ channel flow. The $k-\epsilon$ models are then applied to the problem of three-dimensional flow past

a mounted cube in order to demonstrate the behavior of the hybrid wall treatment in a situation where there are multiple separation/reattachment points and three-dimensional re-circulation zones.

2. Formulation

The Reynolds-averaged Navier-Stokes equations for an incompressible fluid are defined in a domain Ω with boundary $\Gamma = \Gamma_1 \cup \Gamma_2$ in the time interval $[0, T]$.

$$\nabla \cdot \mathbf{v} = 0 \tag{1}$$

$$\frac{\partial \rho \mathbf{v}}{\partial t} + \nabla \cdot (\rho \mathbf{v}\mathbf{v}) = \nabla \cdot (-p\mathbf{I} + \boldsymbol{\tau}) + \rho \mathbf{f} \tag{2}$$

Here, ρ is the mass density, $\mathbf{v} = (v_x, v_y, v_z)^T$ is the velocity, p is the fluid pressure, $\boldsymbol{\tau}$ is the deviatoric laminar and turbulent stress tensor, and $\mathbf{f}$ is the body force per unit mass. A constitutive equation relates the deviatoric stress and the strain rate, $\boldsymbol{\tau} = 2(\mu + \mu_t)\mathbf{S}$, where $\mathbf{S} = \frac{1}{2}[\nabla \mathbf{v} + (\nabla \mathbf{v})^T]$, μ is the moelcular viscosity, and μ_t is the turbulent viscosity.

The momentum equations, Eq. (2), are subject to boundary conditions that consist of prescribed velocity $\mathbf{v}(\mathbf{x}, t) = \hat{\mathbf{v}}(\mathbf{x}, t)$ on Γ_1, or prescribed traction $\mathbf{T} \cdot \mathbf{n} = \hat{\mathbf{f}}(\mathbf{x}, t)$ on Γ_2 where $\Gamma = \Gamma_1 \cup \Gamma_2$ is the domain boundary with outward normal $\mathbf{n}$. A detailed discussion of boundary conditions for the incompressible Navier-Stokes equations may be found in [23]. Velocity initial conditions are prescribed as $\mathbf{v}(\mathbf{x}, 0) = \mathbf{v}^0(\mathbf{x})$. For a mathematically well-posed incompressible flow problem, the prescribed initial and boundary conditions on the velocity field must satisfy

$$\nabla \cdot \mathbf{v}^0 = 0 \tag{3}$$

$$\mathbf{n} \cdot \mathbf{v}(\mathbf{x}, 0) = \mathbf{n} \cdot \mathbf{v}^o(\mathbf{x}) \tag{4}$$

If $\Gamma_2 = 0$, i.e., enclosure flows with $\mathbf{n} \cdot \mathbf{v}$ prescribed on all surfaces, then

$$\int_\Gamma \mathbf{n} \cdot \mathbf{v}^0 d\Gamma = 0 \tag{5}$$

must also be satisfied. The initial pressure is obtained by solving the pressure-Poisson problem associated with initial velocity field (see Christon, et al. [24] for details).

The $k - \epsilon$ transport equations are

$$\frac{\partial \rho k}{\partial t} + \nabla \cdot (\rho \mathbf{v} k) = \nabla \cdot \left(\mu + \frac{\mu_t}{\sigma_k} \nabla k \right) + P_k - D_k \tag{6}$$

$$\frac{\partial \rho \epsilon}{\partial t} + \nabla \cdot (\rho \mathbf{v} \epsilon) = \nabla \cdot \left(\mu + \frac{\mu_t}{\sigma_\epsilon} \nabla \epsilon \right) + P_\epsilon - D_\epsilon \tag{7}$$

where k is the turbulent kinetic energy, and ϵ is the turbulent dissipation rate. The production and dissipation terms are

$$P_k = 2\mu_t \mathbf{S} : \mathbf{S} \tag{8}$$

$$D_k = \rho\epsilon \tag{9}$$

$$P_\epsilon = C_{\epsilon_1}(2\mu_t \mathbf{S} : \mathbf{S})/T_t \tag{10}$$

$$D_\epsilon = C_{\epsilon_2}\rho\epsilon/T_T \tag{11}$$

where the turbulent eddy viscosity is

$$\mu_t = C_\mu \rho k T_t \tag{12}$$

In the $k-\epsilon$ transport equations, the dynamic time-scale k/ϵ has been replaced by the the realizable time-scale of Rahman and Siikonen [2]

$$T_t = \frac{k}{\epsilon}\sqrt{1 + \frac{C_T^2}{Re_T}} \tag{13}$$

where $Re_T = \rho k^2/\nu\epsilon$, and $C_T = \sqrt{2}$. The coefficients for the "standard" and RNG $k-\epsilon$ models are presented in Table 1

Standard $k-\epsilon$ [7]		RNG $k-\epsilon$ [25]	
Model Coefficient	Value	Model Coefficient	Value
C_μ	0.09	C_μ	0.085
σ_k	1.0	σ_k	0.72
σ_ϵ	1.3	σ_ϵ	0.72
$C_{\epsilon 1}$	1.44	$C_{\epsilon 1}$	1.42
$C_{\epsilon 2}$	1.92	$C_{\epsilon 2}$	Eq.(14)
		$\widetilde{C}_{\epsilon 2}$	1.68
		β	0.012
		η_0	4.38

Table 1: Standard and RNG $k-\epsilon$ model coefficients.

where C_{ϵ_2} for the RNG model is defined as

$$C_{\epsilon 2} = \widetilde{C}_{\epsilon 2} + \frac{C_\mu \eta^3 (1 - \eta/\eta_0)}{1 + \beta\eta^3} \tag{14}$$

and

$$\eta = \frac{k}{\epsilon}\sqrt{2\mathbf{S} : \mathbf{S}} \tag{15}$$

The $k-\epsilon$ transport equations are subject to initial and boundary conditions for k and ϵ respectively, and these are discussed in more detail in §2.1. The Navier-Stokes equations are solved using a hybrid second-order projection algorithm as described in [24]. The $k-\epsilon$ transport equations are solved using a second-order spatial discretization with the positivity-preserving linearization outlined in [26]. It is noted in passing that the hybrid projection algorithm used here enjoys a relaxed convective stability condition that permits computations with $CFL > 10$ to be performed for all transport equations.

2.1. Implementation Considerations

The implementation of the two-equation models follows a somewhat typical approach used in many CFD codes. For the turbulent kinetic energy, Eq. (6), boundary conditions are typically of three types. At walls, a homogeneous Neumann condition on the turbulent kinetic energy is applied

$$\frac{\partial k}{\partial n} = 0 \tag{16}$$

This is consistent with the fact that there can not be transport of turbulent kinetic energy to the wall. Additionally, the production of turbulent kinetic energy is computed based on the velocity profile.

For the turbulent dissipation rate, Eq. (7), the wall value is set explicitly based on the specific wall treatment. A penalty technique, at the linear algebra level, enforces the constraint of the dissipation rate in the discrete equations.

At inflow boundaries, a Dirichlet condition may be used if the inlet turbulent kinetic energy and/or dissipation rate are known a priori. Otherwise, a homogeneous Neumann condition may be used which permits the incoming turbulent kinetic energy and dissipation rate to adjust according to the flow conditions. At outflow boundaries, a homogeneous Neumann condition is typically applied for both k and ϵ.

The initial turbulent kinetic energy may be estimated from a known turbulent intensity and velocity as

$$k(\mathbf{x}, 0) = \frac{3}{2}(V_{ref} I)^2 \tag{17}$$

where V_{ref} is the reference (inlet or free stream) velocity, and I is the turbulent intensity. The turbulent intensity is a measure of the RMS velocity fluctuations, v', relative to the reference velocity.

$$I = \frac{v'}{V_{ref}} \tag{18}$$

The turbulent intensity is often inferred from experimental data. The dissipation rate may be estimated a number of ways, but the simplest is based on a viscosity ratio

$$\epsilon(\mathbf{x}, 0) = \rho C_\mu \frac{k^2(\mathbf{x}, 0)}{\mu R} \tag{19}$$

where

$$R = \frac{\mu_t}{\mu} \tag{20}$$

and typically $10 \leq R \leq 100$.

2.2. Scalable Wall Functions

The scalable wall function approach is based on the work of Grotjans and Menter [13] and limits the minimum value of the wall normal coordinate, that

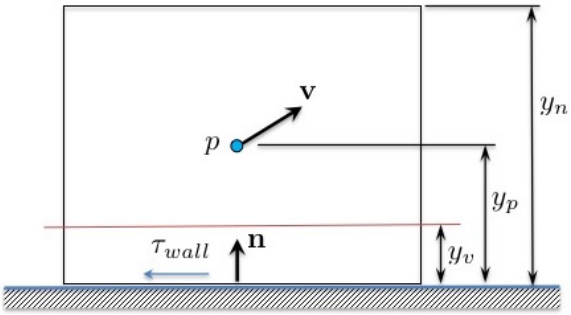

Figure 1: Schematic of the wall element where p is the centroid of the element, y_v and y_p represent the normal distances from the wall to the edge of the viscous sublayer, the element centroid respectively, and y_n is the maximum of the normal distances of all the vertices.

in effect, shifts the velocity profile so that it appears to be at the the edge of the viscous sublayer. This approach neglects the true fluid dynamics within the viscous sublayer, but this is also the case for the standard wall function approach where the formulation breaks down for mesh points within the viscous sublayer. The effect of this shift is discussed further in §3.

To begin the discussion of the scalable wall-function formulation, a representative near-wall element is shown in Fig. 1 along with the various wall normal distances. The non-dimensional wall element centroid distance, y_p, is

$$y_p^* = \frac{C_\mu^{1/4} \rho \sqrt{k} y_p}{\mu}, \tag{21}$$

where, k is the turbulent kinetic energy, ρ is the fluid density, and μ is the molecular viscosity. It is important to note that y^* is scaled with the velocity scale, $C_\mu^{1/4} k^{1/2}$, to avoid singularities when the shear velocity tends to zero, and is common practice in wall treatments.

The scalable wall function is based on the law of the wall

$$v^+ = y^+ + \frac{1}{\kappa} \ln E y^+ \tag{22}$$

where $E = \exp(B\kappa)$, $B = 5.20$ and $\kappa = 0.41$. The edge of the viscous sublayer, y_v, is computed using the intersection of the laminar and logarithmic velocity profiles based on the law of the wall. The corresponding scaled viscous sublayer distance is given by

$$y_v^* = \frac{C_\mu^{1/4} \rho \sqrt{k} y_v}{\mu} = 11.225 \tag{23}$$

In order to ensure that the wall conditions are effectively at the edge of the viscous sublayer, the following limiter is used

$$y_{plim}^* = \max\left(y_p^*,\ y_v^*\right). \tag{24}$$

The value of y_p is calculated as

$$y_{p_{lim}} = \frac{y^*_{p_{lim}}\mu}{C_\mu^{1/4}\rho\sqrt{k}} \tag{25}$$

In order to estimate the production of turbulent kinetic energy in the wall-attached element, the procedure outlined in Craft et al. [14] is adopted. The production rate is assumed to be negligible in the viscous sublayer, $y \leq y_v$, shown in Fig. 1. The production rate of k in the logarithmic layer and the viscous sublayer are

$$P_k = \begin{cases} 0 & \text{for } \; y_p^* < y_v^* \text{ (Dissipation Layer)} \\ \dfrac{\tau_{wall}^2}{\kappa C_\mu^{1/4}\rho k^{3/2} y} & \text{for } \; y_p^* \geq y_v^* \text{ (Logarithmic Layer)} \end{cases} \tag{26}$$

where,

$$\tau_{wall} = \frac{\kappa C_\mu^{1/4}\rho \; V_p\sqrt{k}}{\ln(E y_p^*)}. \tag{27}$$

Here, V_p is the wall-tangent velocity evaluated at the cell centroid p as

$$V_p = \| \; (\mathbf{v} - \mathbf{v}_{wall}) - \Big[(\mathbf{v} - \mathbf{v}_{wall}) \cdot \mathbf{n}\Big]\mathbf{n} \; \| \tag{28}$$

where $\mathbf{n}$ is the wall normal based on the cell face, and $\mathbf{v}_{wall}$ is a relative wall velocity.

Since P_k varies in the wall-normal direction as shown in Eq. (26), an average value of P_k denoted by $\overline{P_k}$ is used in the k-transport equation. In the implementation, integration along the wall normal distance, y, is performed to obtain $\overline{P_k}$ with the averaging limits for y taken to be 0 and y_n (see, Fig. 1). Here, y_n is the maximum of the wall normal distances of all the vertices in a given wall element. In the present formulation, $y_n \approx 2y_p$.

The average production rate is

$$\begin{aligned} \overline{P_k} &= \frac{1}{y_n}\int_0^{y_n} P_k dy \\ &= \underbrace{\frac{1}{y_n}\int_0^{y_v} P_k dy}_{\text{Viscous sublayer}} + \underbrace{\frac{1}{y_n}\int_{y_v}^{y_n} P_k dy}_{\text{Logarithmic layer}} \end{aligned} \tag{29}$$

Using Eq.(26) in Eq.(29), $\overline{P_k}$ is

$$\overline{P_k} = \frac{\tau_{wall}^2}{\kappa C_\mu^{1/4}\rho k^{1/2} y_n} \ln\left(\frac{y_n}{y_v}\right) \tag{30}$$

where $\overline{P_k}$ is used in place of P_k in Eq.(7) for wall-attached elements at no-slip/no-penetration boundaries.

Similar to $\overline{P_k}$, an average dissipation rate of k, $\overline{D_k}$, is evaluated using the variation of ϵ as suggested by Craft, et al. [14]. The assumed variation is shown in Fig. 2 and is expressed as

$$\epsilon = \begin{cases} \dfrac{2\nu k}{y_v^2} & \text{for} \quad y_p^* \le y_v^* \\ \dfrac{C_\mu^{3/4} k^{3/2}}{\kappa y} & \text{for} \quad y_p^* > y_v^* \end{cases} \tag{31}$$

where $\nu = \mu/\rho$. This implies that

$$D_k = \rho\epsilon = \begin{cases} \dfrac{2\mu k}{y_v^2} & \text{for} \quad y_p^* \le y_v^* \\ \rho\dfrac{C_\mu^{3/4} k^{3/2}}{\kappa y} & \text{for} \quad y_p^* > y_v^* \end{cases} \tag{32}$$

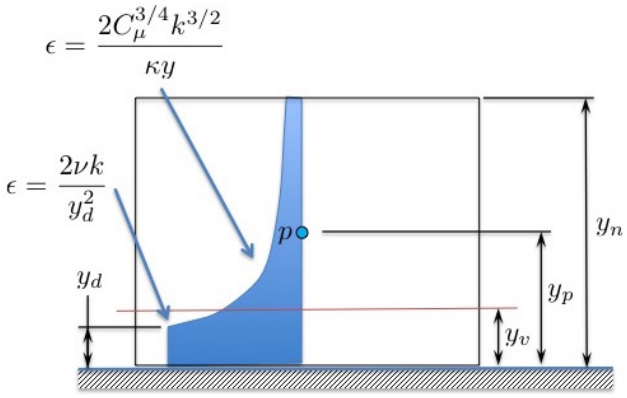

Figure 2: Schematic of the assumed ϵ variation in the wall elements.

Similar to $\overline{P_k}$, the depth-averaged dissipation rate is

$$\begin{aligned} \overline{D_k} &= \frac{1}{y_n}\int_0^{y_n} D_k dy \\ &= \underbrace{\frac{1}{y_n}\int_0^{y_d} D_k dy}_{\text{Viscous sublayer}} + \underbrace{\frac{1}{y_n}\int_{y_d}^{y_n} D_k dy}_{\text{Turbulent log-layer}} \end{aligned} \tag{33}$$

Using Eq. (32) and Eq. (33), the average dissipation rate is

$$\overline{D_k} = \frac{2\mu k}{y_n y_d} + \frac{\rho C_\mu^{3/4} k^{3/2}}{\kappa y_n} \ln\left(\frac{y_n}{y_d}\right). \tag{34}$$

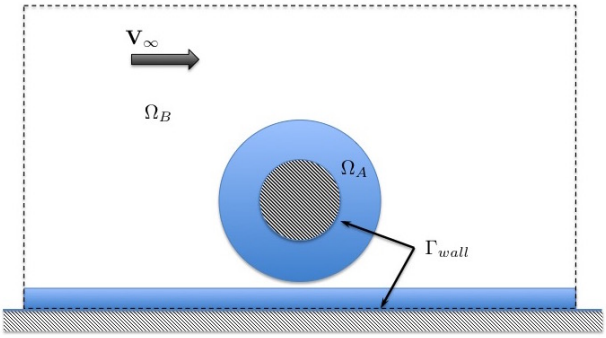

Figure 3: Schematic of the two-layer segregation of the flow domain into regions Ω_A for the fully-turbulent region, and Ω_B for the near-wall region.

where

$$y_d = \frac{\mu\kappa}{\rho C_\mu^{3/4} k^{1/2}} \tag{35}$$

The dissipation rate, Eq. (7), is specified in wall-attached elements using the limited normal distance, $y_{p_{lim}}$, as

$$\epsilon = \frac{C_\mu^{3/4} k^{3/2}}{\kappa y_{p_{lim}}} \tag{36}$$

Numerically, this is implemented using a penalty technique to enforce the cell-centered value of the dissipation rate.

Finally, the viscosity at the no-slip/no-penetration wall is evaluated as

$$\mu_{\text{wall}} = \frac{\rho C_\mu^{1/4} k^{1/2} \kappa y_p}{\ln\left(E y^*_{p_{lim}}\right)} \tag{37}$$

2.3. Hybrid Two-Layer Treatment

The hybrid two-layer treatment is based, in part, on the work by Chen and Patel [11]. The two-layer implementation requires that the cells in the flow domain be segregated dynamically (on-the-fly) based on the local turbulent Reynolds number as shown in Fig. 3. The turbulent Reynolds number is defined as

$$Re_y = \frac{\rho k^{1/2} y}{\mu} \tag{38}$$

The delineation between the near-wall and fully-turbulent regions is based on a specified threshold Re_y^*. Cells where $Re_y \leq Re_y^*$ are segregated into the near-wall layer (Ω_A), while all others are relegated to the fully-turbulent portion (Ω_B) of the domain.

In the near-wall layer, the turbulent eddy viscosity is computed using the turbulent Reynolds number

$$\mu_{t_A} = \mu Re_y C_\mu^{3/4} \kappa \left\{ 1 - \exp\left(\frac{-Re_y}{A_\mu} \right) \right\} \tag{39}$$

where $A_\mu = 70$. The dissipation rate is computed from a dissipation length scale

$$\epsilon_A = \frac{k^{3/2}}{l_\epsilon} \tag{40}$$

where

$$l_\epsilon = C_l y \left\{ 1 - \exp\left(\frac{-Re_y}{A_\epsilon} \right) \right\} \tag{41}$$

$A_\epsilon = 2C_l$, and $C_l = \kappa / C_\mu^{3/4}$. Similar to the scalable wall function approach, the values of ϵ_A are set using a penalty method at all elements that are identified as being in the near-wall region Ω_A.

In order to smoothly transition from the near-wall layer to the fully-turbulent layer the blending function suggested by Jongen [27] is used for the turbulent viscosity.

$$\mu_t = \lambda_\epsilon \mu_{t_B} + (1 - \lambda_\epsilon) \mu_{t_A} \tag{42}$$

where

$$\lambda_\epsilon = \frac{1}{2} \left\{ 1 + \tanh\left(\frac{Re_y - Re_y^*}{A} \right) \right\} \tag{43}$$

The constant, A, determines the width of the blending function, while Re_y^* determines the location of the blending function. Given Re_y^*, A is computed by requiring that $\lambda_\epsilon = 0.99$ when $Re_y - Re_y^* = \alpha Re_y^*$ where $0.05 \leq \alpha \leq 0.15$.

Testing the location and width of the blending function has shown that, in general, calculations are relatively insensitive to the value of α. However, the choice of Re_y^* is somewhat more important because a small value will result in the blending occurring in the buffer or laminar sublayer of the the boundary layer. In contrast, too large a value will place the blending function in the fully-turbulent region. In general, the choice of Re_y^* should place the blending function as close to the wall as possible while preserving the laminar sublayer. Figure 4 shows the variation of the blending function with respect to Re_y^* and α. After exhaustive testing on both equilibrium and non-equilibrium flows, $Re_y^* = 75$, $\alpha = 0.15$ has been selected. As an aside, it should be noted that Re_y^* and α are model parameters and should not be viewed as user-defined coefficients.

Turning attention to the remaining conditions for the velocity and wall turbulent viscosity, there are several choices available for the construction of a wall law with a buffer region. The wall profile of Kader [22] is

$$v^+ = e^\Gamma y^+ + e^{1/\Gamma} \frac{\ln(Ey^+)}{\kappa} \tag{44}$$

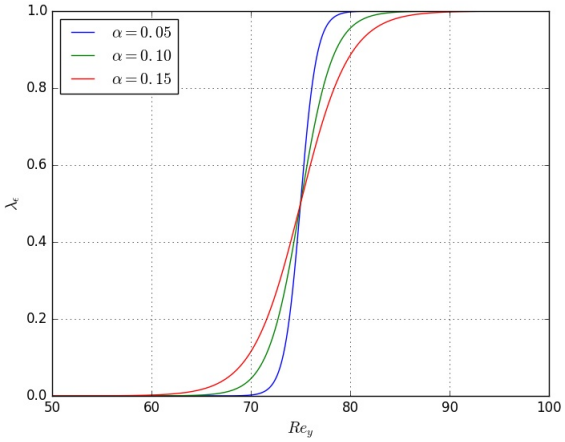

Figure 4: Jongen blending function for turbulent viscosity with varying α.

where

$$\Gamma = \frac{0.01{y^+}^4}{1 + 5y^+} \tag{45}$$

The second option considered here is due to Reichardt [28]

$$v^+ = \frac{1}{\kappa} \ln\left(1 + \kappa y^+\right) + 7.8 \left\{ 1 - \exp\left(\frac{-y^+}{11}\right) - \frac{y^+}{11} \exp\left(\frac{-y^+}{3}\right) \right\} \tag{46}$$

Figure 5 shows the linear, logarithmic, Kader and Reichardt velocity profiles. The Kader profile exhibits clear defects and under-predicts the velocity in the region $3 \leq y^+ \leq 10$. Despite this, testing has not shown a significant difference between the two velocity profiles. However, for this work, the Reichardt profile was chosen.

In order to make use of the non-dimensional Reichardt profile, the following relationships (see Launder and Spalding [7]) are required.

$$y^+ = \frac{\rho y v^*}{\mu} \tag{47}$$

$$v^+ = \frac{\rho v v^*}{\tau_{wall}} \tag{48}$$

where the reference velocity, v^*, is

$$v^* = \sqrt{\frac{\mu V_p}{\rho y_p} + C_\mu^{1/2} k_p} \tag{49}$$

and V_p is computed using Eq. (28).

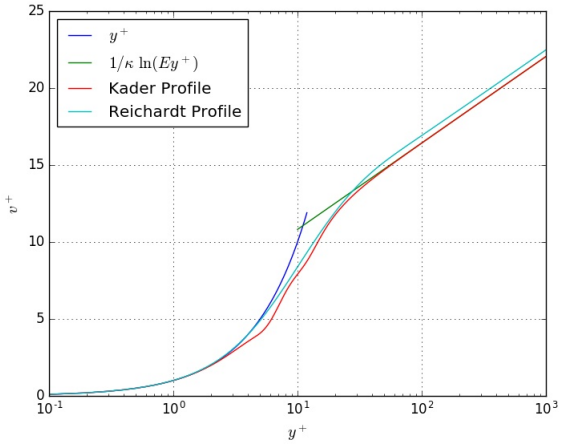

Figure 5: Linear, logarithmic, Kader and Reichardt velocity profiles.

Rearranging Eq. 48, the wall shear stress can be written in terms of V_p, y_p permitting the direct computation of the wall turbulent eddy viscosity

$$\mu_w = \frac{\rho v^* y_p}{v^+} \tag{50}$$

where $v+$ is simply the Reichardt velocity profile (or alternatively the Kader profile). Expanding the reference velocity yields

$$\mu_w = \frac{\rho\sqrt{\frac{\mu V_p}{\rho y_p} + C_\mu^{1/2} k_p} y_p}{v^+} \tag{51}$$

Turning now to the production of turbulent kinetic in the near-wall cell, the production may be written in terms of the non-dimensional velocity, the velocity gradient, and the reference velocity as

$$P_k = \frac{1}{\mu}\left(\frac{\rho v^* V_p}{v^+}\right)\left\{\left(\frac{v^* v+}{V_p}\right) - \frac{\partial v^+}{\partial y^+}\right\}\frac{\partial v^+}{\partial y^+} \tag{52}$$

where for the Reichardt velocity,

$$\frac{\partial v^+}{\partial y^+} = \frac{1}{1+\kappa y^+} + 7.8\left\{\frac{1}{11}\exp\left(\frac{-y^+}{11}\right) + \left(\frac{y^+}{33} - \frac{1}{11}\right)\exp\left(\frac{-y^+}{3}\right)\right\} \tag{53}$$

Similar to the scalable wall function treatment, the dissipation of turbulent kinetic energy is computed as an average using

$$\overline{D_k} = \frac{1}{y^n}\int_0^{y_n} \frac{\rho C_\mu^{3/4} k_p^{3/2}}{\kappa y_p\left\{1 - \exp\left(\frac{-\rho k_p^{1/2} y_p}{\mu A_\epsilon}\right)\right\}} dy \tag{54}$$

3. Results

In order to assess the scalable and hybrid two-layer wall treatments, a series of calculations beginning with a $Re_\tau = 590$ channel flow are compared to the DNS data of Moser, et al. [29]. In order to gauge the behavior of the scalable and hybrid wall functions with both the STD and RNG $k-\epsilon$ models, the one-equation Spalart-Allmaras model [30] is used on the same suite of grids. Following the channel flow studies, the hybrid wall treatment is used with the standard and RNG models to compute the flow past a mounted cube in order to assess the behavior of the wall modeling approach in a situation with multiple separation/reattachment points and three-dimensional re-circulation zones.

3.1. $Re_\tau = 590$ Channel Flow

The channel flow problem is non-dimensional and uses a computational domain that is is 20×1 units. Homogeneous Neumann boundary conditions for $\mathbf{v}$, k and ϵ are used at the inflow/outflow boundaries. The inflow pressure is $p = 0.557$, and the outflow pressure is $p = 0.0$. No-slip/no-penetration velocity boundary conditions are imposed at the top/bottom boundaries of the channel. The initial conditions consist of is $\mathbf{v}(\mathbf{x}, 0) = \mathbf{0}$, $k(\mathbf{x}, 0) = 0.015$, $\epsilon(\mathbf{x}, 0) = 0.002$. This choice of boundary conditions permits the velocity, k and ϵ to evolve without any significant entrance effects to the channel. The non-dimensional density is $\rho = 1$, and the molecular viscosity is $\mu = 1.0e-4$. For the Spalart-Allmaras model, the initial conditions are $\tilde{\nu} = 3.1e-4$, and again, homogeneous Neumann inflow/outflow conditions are used.

In order to assess the behavior of the wall treatment, an initial study was performed using uniform mesh spacing with a series of six levels of grid refinement as shown in Table 2 for Mesh-A – Mesh-F. This mesh refinement strategy was chosen to force the near wall mesh point to pass from the fully-turbulent region through the buffer layer and into the laminar sublayer. Next a mesh refinement study that initially placed the first mesh point in the laminar sublayer was used. Here, exponential grading in the wall-normal direction was used while constraining a uniform refinement of the wall-attached cells as shown in in Table 2 for Mesh-G – Mesh-J.

All computations using the Spalart-Allmaras model, and $k-\epsilon$ models with the hybrid wall treatment were performed using a backward-Euler time-integrator, with a fixed time-step $\Delta t_{max} = 0.2$. In contrast, the use of the scalable wall functions exhibited a reduced stability limit, and all computations were performed using $\Delta t_{max} = 0.1$. Each calculation was instrumented to collect time-history velocity, pressure, and global kinetic energy ($\frac{1}{2}\int_\Omega \rho \mathbf{v} \cdot \mathbf{v}$) data to determine the presence of a steady-state solution.

Spalart-Allmaras

The global kinetic energy time-history data for Mesh-A – Mesh-J are shown in Fig. 6. The global kinetic energy plots indicate that all computations exhibited steady-state behavior by $t = 500$ time units, and the velocity/pressure time-history data confirmed this behavior. For Mesh-A and Mesh-B, the $y+$

Mesh	(N_x, N_y)	$(\Delta x,\ \Delta y_{min})$	y^+_{min}
Mesh-A	(50, 11)	(4.0e-2, 9.0909e-2)	53.636
Mesh-B	(50, 21)	(4.0e-2, 4.7619e-2)	28.095
Mesh-C	(50, 41)	(4.0e-2, 2.4390e-2)	14.390
Mesh-D	(50, 81)	(4.0e-2, 1.2346e-2)	7.2839
Mesh-E	(50, 161)	(4.0e-2, 6.2112e-3)	3.6646
Mesh-F	(50, 321)	(4.0e-2, 3.1153e-3)	1.8380
Mesh-G	(50, 51)	(4.0e-2, 5.0847e-3)	3.0000
Mesh-H	(50, 101)	(4.0e-2, 2.5424e-3)	1.5000
Mesh-I	(50, 201)	(4.0e-2, 1.2712e-3)	0.7500
Mesh-J	(50, 401)	(4.0e-2, 6.3556e-4)	0.3750

Table 2: Mesh resolution for the $Re_\tau = 590$ channel flow showing the cell count, and mesh spacing in terms of the cell size and y^+ at the no-slip/no-penetration walls.

associated with the first mesh point was insufficient, and the Spalart-Allmaras (SA) model grossly over-predicted the velocity field. This is to be expected as the model, as implemented, is strictly a low-Re model requiring $y+ \leq 10$. As indicated in Fig. 6(a), the behavior of the kinetic energy, and consequently the velocity field, under mesh refinement is non-monotonic as the first mesh point passes through the buffer layer and into the laminar sublayer, i.e., for Mesh-C through Mesh-F. In contrast, convergence behavior when the first mesh point is always in the laminar sublayer is monotonic as shown by the asymptotic kinetic energy values in Fig. 6. This behavior is also shown in Fig. 12.

The velocity profiles for the mesh study are shown in Fig. 7 with the DNS data of Moser, et al. [29]. Again, the non-monotonic behavior for the uniform mesh refinement study is seen in Fig. 7(a) with Mesh-C over-predicting the velocity profile, while Mesh-D – Mesh-E under-predict the velocity profile particularly for $y+ \geq 10$. In contrast, a more monotonic behavior is seen in Fig. 7(b) when there are multiple mesh points in the laminar sublayer. This overall behavior is not surprising given the low-Re nature of the Spalart-Allmaras model, but it does give insight into the use of grids that are either under-resolving the boundary layer, or in the case of complex geometries, where the near-wall mesh resolution varies spatially and does not permit $y+ \leq 10$ at all locations along walls.

Scalable Wall-Function

Turning to the scalable wall functions, Fig. 8 shows the global kinetic energy time history plots for the standard and RNG models. In contrast to the Spalart-Allmaras results, the scalable wall function treatment appears to behave in a more monotonic fashion under mesh refinement. Inspection of the velocity profiles in Fig. 9 does indicate that under mesh refinement, the velocity profile in the region $y+ \geq 10$ does increase monotonically. However, the real problem with this wall treatment is clear for $y+ < 10$ where the offset in the velocity

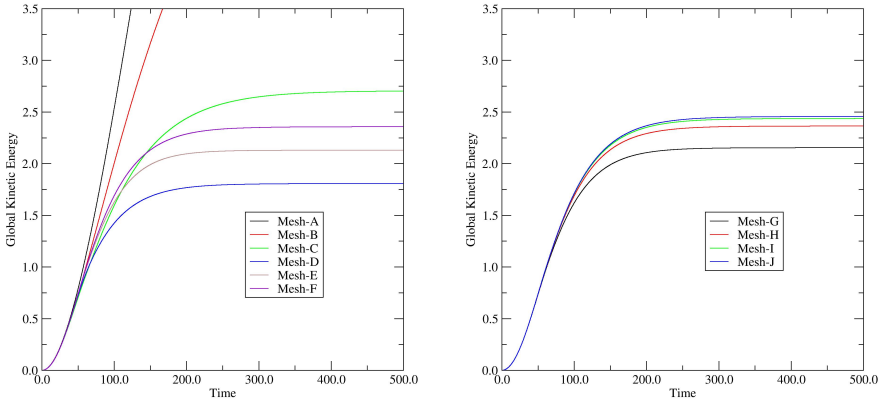

(a) (b)

Figure 6: Global kinetic energy ($\frac{1}{2}\int_\Omega \rho \mathbf{v}\cdot\mathbf{v}$) for the Spalart-Allmaras model using (a) uniform refinement on meshes A-F, and (b) refinement of $y+$ at the wall for meshes G-J.

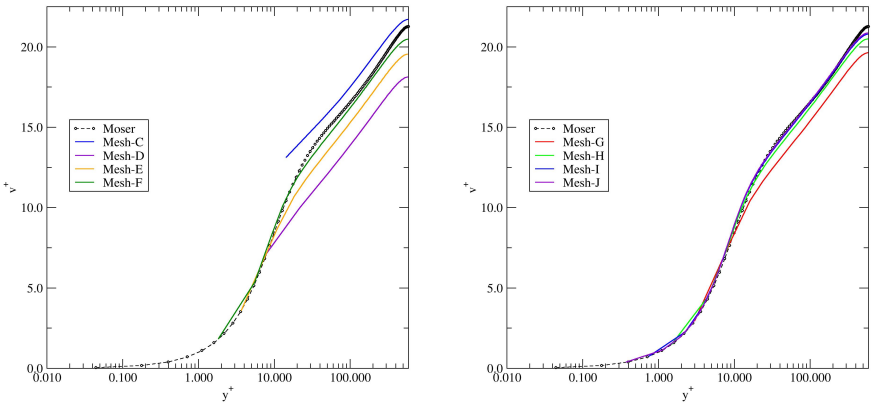

(a) (b)

Figure 7: Velocity profile for the Spalart-Allmaras model using (a) uniform refinement on meshes C-F, and (b) refinement of $y+$ at the wall for meshes G-J.

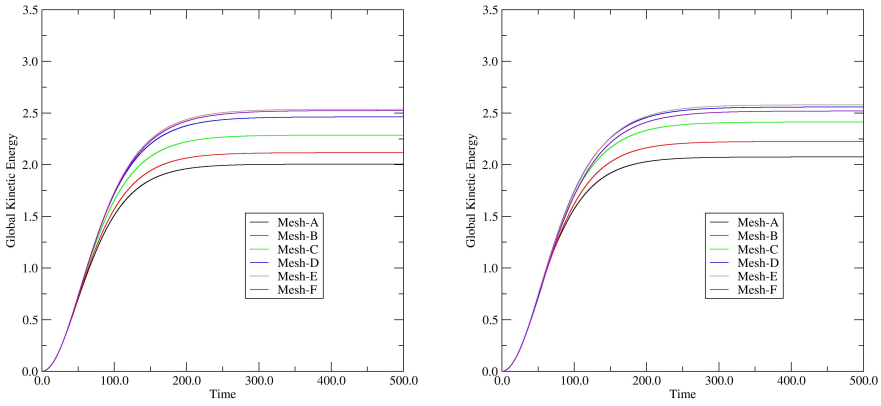

Figure 8: Global kinetic energy ($\frac{1}{2}\int_\Omega \rho \mathbf{v}\cdot\mathbf{v}$) for (a) the standard $k-\epsilon$ model and (b) the RNG model using the scalable wall functions with meshes A-F.

profile is observed. So, on the face of it, the scalable wall functions appear robust in terms of the near-wall meshing, but the solution converges to a velocity profile that is completely incorrect in the laminar sublayer due to the velocity shift.

For problems with complex geometry, where a high Reynolds number approach is warranted, and near-wall mesh points can not be strictly controlled to guarantee $y+ > 30$, the scalable wall treatment may prove useful. However, mesh refinement studies for verification may prove problematic in general, and for problems where wall shear stress or heat transfer is important, this is not a viable approach. Thus, the scalable wall functions are dropped from further examination.

Hybrid Two-Layer Treatment

The global kinetic energy time-history plots for the standard (STD) and RNG $k-\epsilon$ models using the hybrid two-layer wall treatment are shown in Fig. 10. The STD and RNG models both exhibit non-monotonic behavior in terms of the global kinetic energy with respect to mesh refinement until there are mesh points located in the buffer region or laminar sublayer ($y+ <\sim 10$). The RNG model tends to result in somewhat more energetic velocity fields, with larger maximal x-velocity at the channel centerline as shown in Fig. 10(c). This is also seen in Fig. 11(c) where RNG over predicts the velocities for Mesh-A and Mesh-B. The STD model tends to show less deviation from the DNS data for Mesh-A – Mesh-F in comparison to the RNG results.

In contrast to the Spalart-Allmaras model, both the STD and RNG models deliver reasonable velocities for the coarse meshes, even on Mesh-A which provides only 11 mesh points across the channel. The disparity between the

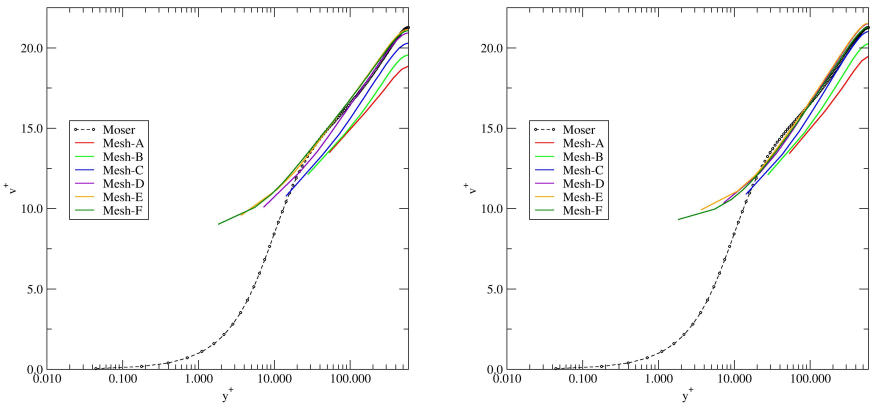

(a) (b)

Figure 9: Velocity profile for (a) the standard $k-\epsilon$ model and (b) the RNG model using the scalable wall functions with meshes A-F.

coarsest and finest meshes is more apparent with RNG. Again, using Mesh-G – Mesh-J, the convergence becomes monotonic as the laminar sublayer is resolved for both the RNG and STD models.

Turning to the convergence behavior, Fig. 12(a) shows the behavior of the asymptotic global kinetic energy (at $t = 500$ time units) as a function of the y^+ in the wall-attached element. The Spalart-Allmaras model requires $10 \leq y^+ \leq 15$ before the velocity profile begins to approach the DNS data as shown in in Fig. 7(a). In contrast the $k-\epsilon$ models using either the scalable and hybrid wall treatments deliver "reasonable" velocity profiles for relatively coarse meshes. Although the scalable wall functions appear to behave in a convergent manner, mesh points placed below the edge of the viscous sublayer do not provide any real benefit in terms of accuracy.

The asymptotic kinetic energy plots in Fig. 12(b) show a near-quadratic convergence in terms of $y+$. Richardson extrapolation was used to estimate the order of convergence for the three models using meshes H – J as shown in Table 3. Although all three are nearly second-order in terms of the asymptotic global kinetic energy metric, it is noted that the three are models, and the velocity profiles can not be expected to be identical even on the finest mesh (see Fig. 7(b), 11(b) and (d)).

Model	Convergence Rate
Spalart-Allmaras	1.84
Standard $k-\epsilon$ – Hybrid 2-Layer	1.78
RNG $k-\epsilon$ – Hybrid 2-Layer	1.70

Table 3: Convergence rate estimates using Meshes H–J.

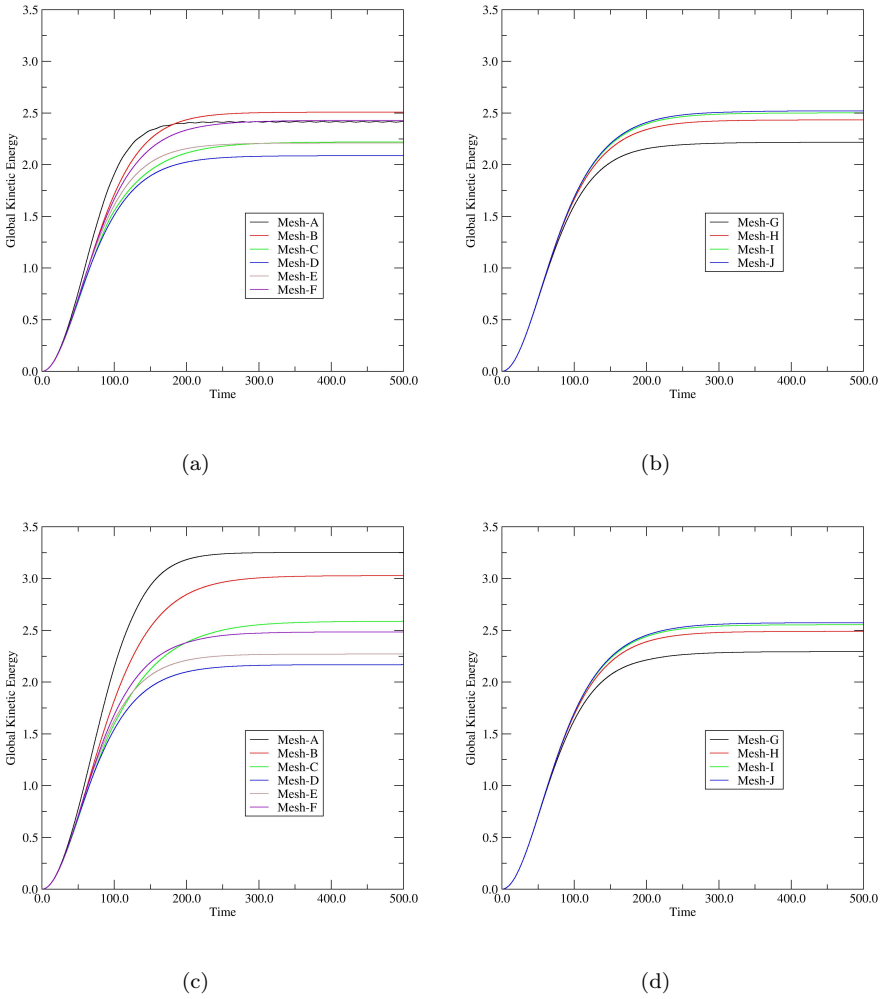

Figure 10: Global kinetic energy ($\frac{1}{2}\int_\Omega \rho \mathbf{v}\cdot\mathbf{v}$) for $k-\epsilon$ model with the hybrid two-layer wall treatment using (a) the standard model with uniform refinement on meshes A–F, (b) the standard model with refinement of the $y+$ at the wall for meshes G–J, (c) the RNG model with uniform refinement on meshes A–F, and (d) the model with refinement of the $y+$ at the wall for meshes G–J.

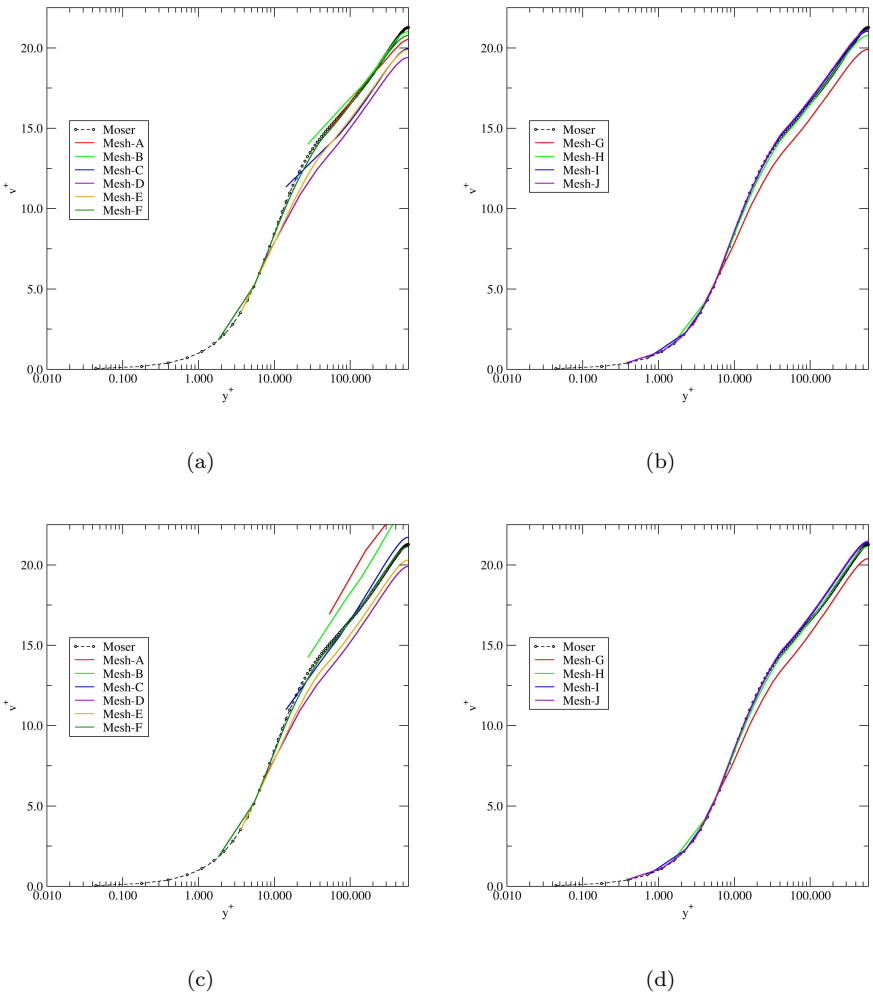

Figure 11: Velocity profile for the standard and RNG $k-\epsilon$ models with the hybrid two-layer wall treatment using (a) uniform refinement on meshes A-F, and (b) refinement of the $y+$ at the wall for meshes G-J.

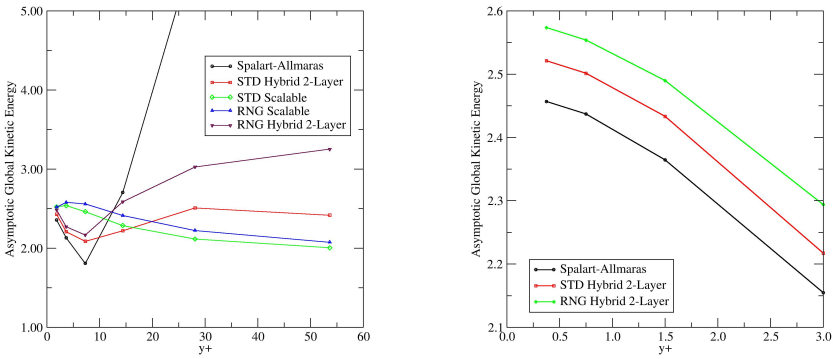

(a) (b)

Figure 12: Asymptotic global kinetic energy ($\frac{1}{2}\int_\Omega \rho \mathbf{v}\cdot\mathbf{v}$) for the Spalart-Allmaras, standard and RNG $k-\epsilon$ models using (a) uniform refinement on meshes A-F, and (b) refinement of the $y+$ at the wall for meshes G-J.

3.2. Mounted Cube

Next, attention is turned to flow past a surface mounted cube in turbulent channel flow. The standard and RNG $k-\epsilon$ models using the hybrid two-layer wall treatment are used, and the computed results compared to the the experimental data by Meinders, et al. [31] and the DNS results by Yakhot, et al. [32]. The geometry for the flow domain is adopted from [32] as shown in Fig. 13. The Reynolds number is based on the cube height, h, and for the laser-Doppler data reported by Meinders, et al., $Re_h = 4400$. In contrast, Yahkot, et al., performed their DNS at $R_h = 1870$. For this work, the $k-\epsilon$ models are exercised at both Reynolds numbers.

The computational mesh contains 2.225×10^6 hex elements and is highly graded to provide reasonable boundary layer resolution on the channel and cube surfaces with $0.18 \leq y^+ \leq 4.5$. The inlet velocity profile is based on the semi-empirical channel flow profile described by White [33] (pp. 458 – 463) as a traditional 1/7th power-law profile was not adequate. No-slip/no-penetration conditions are prescribed at the top/bottom surfaces of the channel and the mounted cube. At the inflow, homogeneous Neumann conditions are used for k and ϵ, while $p = 0$ at the outflow. The velocity initial conditions are obtained by computing an initial divergence-free velocity field that is consistent with the boundary conditions. The initial pressure is obtained by solving the pressure-Poisson problem associated with initial velocity field (see Christon, et al. [24] for details). The initial turbulent kinetic energy was estimated to be $k(\mathbf{x}, 0) = 1.35e-3$, while $\epsilon(\mathbf{x}, 0) = 0.6195$.

Initially a second-order trapezoidal time integrator was used to test the

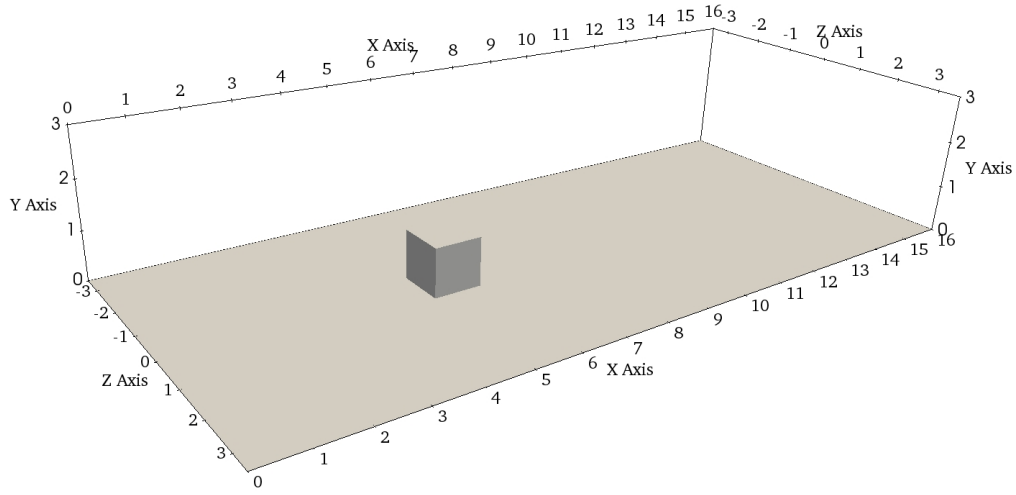

Figure 13: Geometry for mounted cube mesh.

sensitivity of the flow for a variety of time-step sizes. All computations indicated that the flow achieved a steady-state at approximately 200 time units. For the remaining calculations, a backward-Euler time integrator was used with $\Delta t_{max} = 0.2$ time units. Figure 14(a) shows the global kinetic energy time history for the STD and RNG models for the Re_h considered here. Time-history data at points just downstream of the mounted cube, $\mathbf{x} = (6.5, 0.5, \pm 0.5)$ and $\mathbf{x} = (6.5, 0.75, \pm 0.5)$, were used to assess the steady-state conditions as well. Figure 14(b) shows the x-velocity time histories. All computations were carried out to 500 time units to ensure a steady-state condition had been achieved.

The primary vortical structures may be identified by the particle traces shown in Fig. 15(a). The region in front of the cube is associated with a horse-shoe vortex that wraps around the cube, while the re-circulation zones on the top, sides and downstream of the cube may be easily identified. The streak-lines on the channel floor shown in Fig. 15(b) correlate well with the results in Yakhot, et al. [32] and clearly indicate multiple separation and reattachment points along with strong re-circulation zones downstream of the mounted cube.

In order to compare with the data of Meinders, et al. [31] and Yakhot, et al. [32], high-resolution velocity data was collected along the x-axis at $y/h = 0.1, 0.3, 0.5, 0.7, 0.9$ as shown in Fig. 16. The $Re_h = 1870$ results in Fig. 16(a–c) match those of Yakhot quite well, although the strength of the re-circulation zone in front of the mounted cube is under-predicted. This is identified by the under-prediction of the minimum velocity for $y/h = 0.1$ for $4.5 \leq x \leq 5$). In contrast, the agreement with the separated region just behind the cube is reasonable for both the $Re_h = 1870$ and $Re_h = 4400$ up to approximately

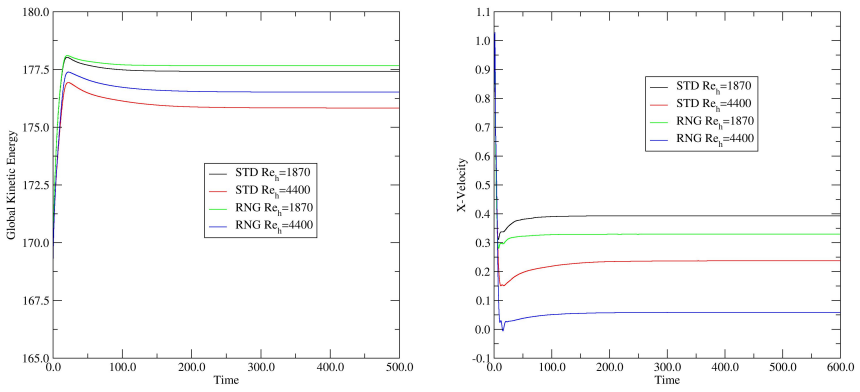

(a) (b)

Figure 14: Time-history plots for the mounted cube: (a) global kinetic energy time-history plot for the standard and RNG $k-\epsilon$ models, (b) velocity time-histories at $(6.5, 0.5, \pm 0.5)$.

$x = 7.0$. Beyond this point, the recovery in the x-velocity, downstream of the cube, is under-predicted. It is noted in passing that the RNG model again appears to produce slightly more "energetic" velocities.

The delayed recovery can be understood, in part, by examining the turbulent eddy-viscosity downstream of the mounted cube. Figure 17 shows the ratio of the turbulent eddy-viscosity to the molecular viscosity. The peak turbulent eddy viscosity appears upstream of the mounted cube for the STD model as shown in Fig. 17(a) and (c). In contrast, the RNG model appears to produce a region of reduced eddy viscosity near the top of the cube which propagates downstream. This explains, in part, the "energetic" behavior observed in the velocities. However, for both the STD and RNG models, the eddy-viscosity increases in the wake behind the mounted cube and is likely the culprit for the delayed viscosity recovery.

4. Summary and Conclusions

This work has examined the behavior of the so-called "scalable" wall functions and a new hybrid two-layer wall treatment in the context of variable mesh resolution in order understand the behavior of the standard and RNG $k-\epsilon$ models as the near wall mesh point moves from the fully-turbulent region, through the buffer zone, and into the laminar sublayer. Although the scalable wall functions may be "robust" in terms of delivering results for any near-wall mesh resolution, the approach is really still a high-Reynolds number method. Unfortunately, using the scalable wall functions, the velocity profile for simple channel flow does not even begin to resolve the laminar sublayer even when $y+ < \sim 10$.

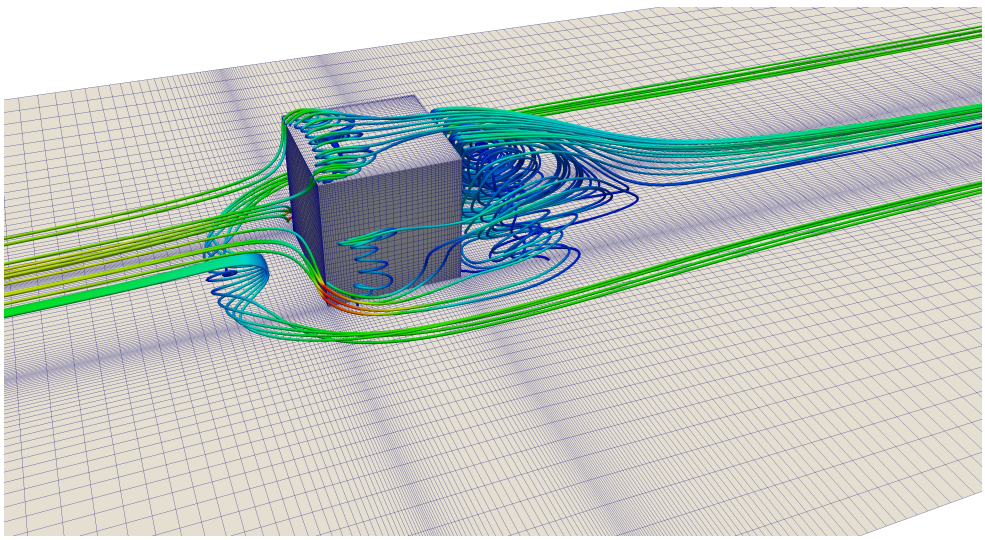

(a)

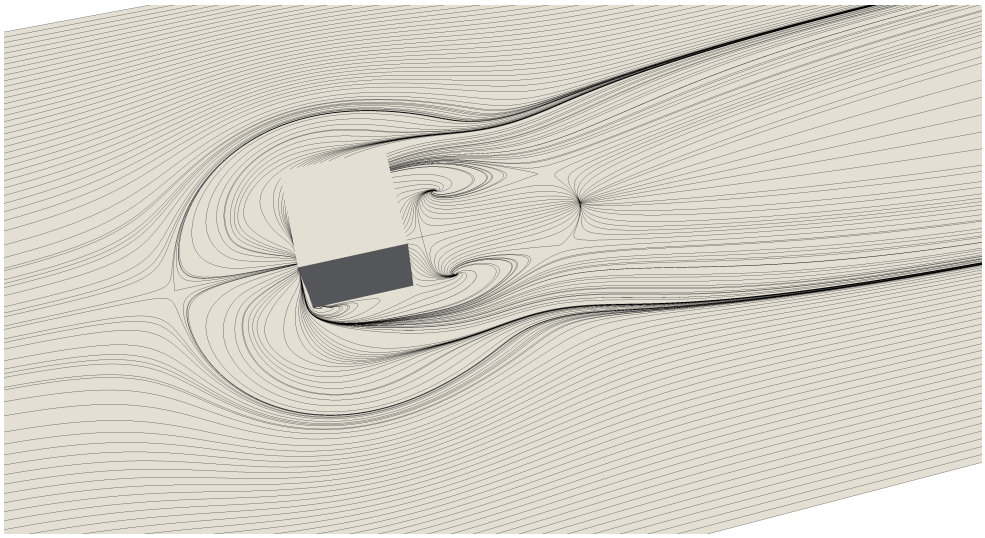

(b)

Figure 15: Flow past the mounted cube at $Re_h = 1870$ showing (a) particle traces colored by velocity magnitude, and (b) streaklines on the bottom channel wall at $y/h = 0.003$.

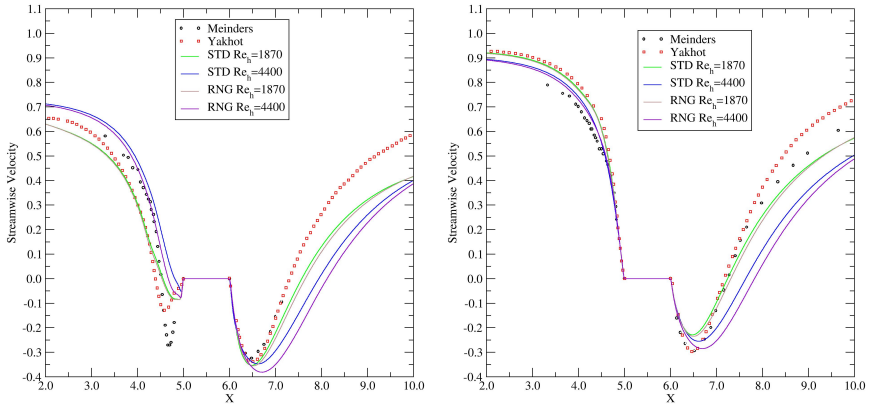

(a)

(b)

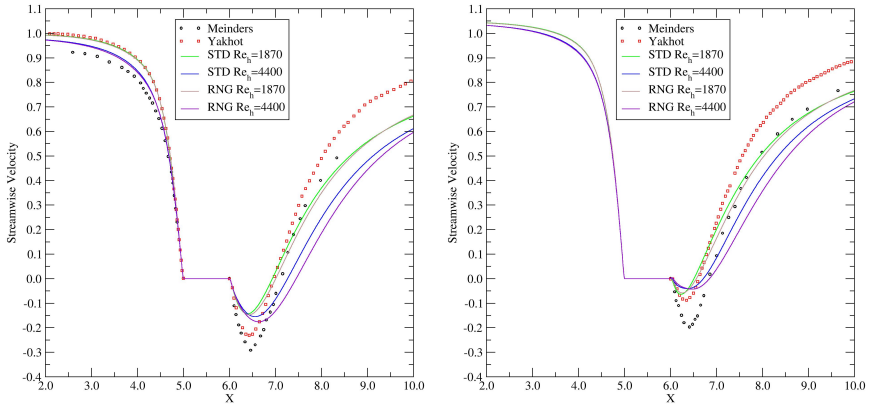

(c)

(d)

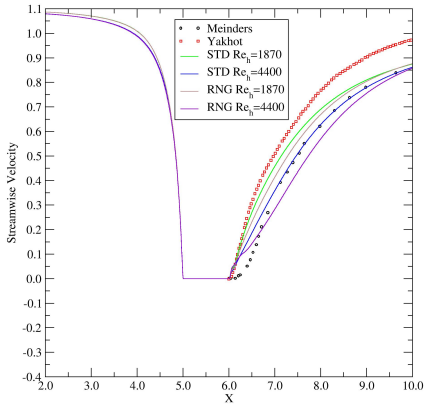

(e)

Figure 16: Streamwise velocity profiles for the standard $k-\epsilon$ models using the hybrid two-layer wall treatment at (a) $y/h = 0.1$, (b) $y/h = 0.3$, (c) $y/h = 0.5$, (d) $y/h = 0.7$, and (e) $y/h = 0.9$.

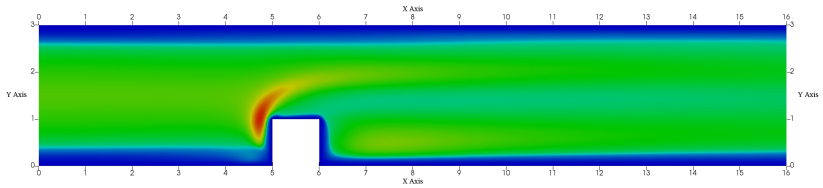

(a)

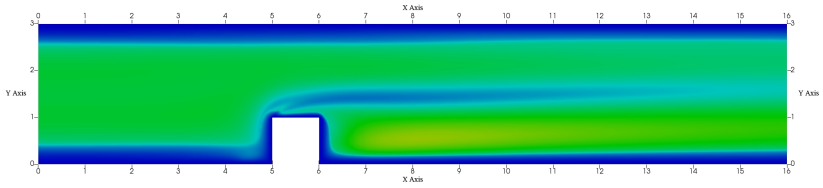

(b)

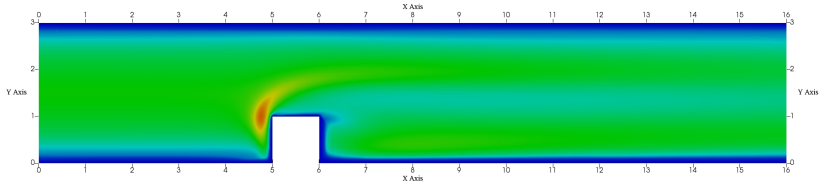

(c)

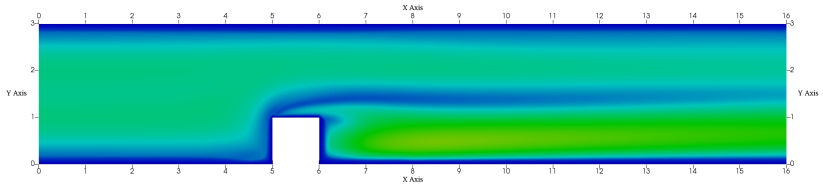

(d)

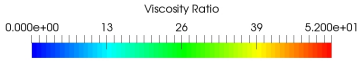

Figure 17: Cut-plane at $z/h = 0.0$ showing ν_t/ν for (a) standard model with $Re_h = 1870$, (b) RNG model with $Re_h = 1870$, (c) standard model with $Re_h = 4400$, and (d) RNG model with $Re_h = 4400$.

In contrast, the hybrid two-layer wall treatment delivers a convergent model, albeit still a model, that can resolve into the laminar sublayer. Relative to the low-Reynolds number Spalart-Allmaras model, the hybrid wall treatment provides the desired doubly-asymptotic behavior for the standard and RNG $k-\epsilon$ models. The sensitivity with respect to the placement of the near-wall mesh points is slightly more pronounced for the RNG model than the standard $k-\epsilon$ model, although both suffer from excessive dissipation downstream of the mounted cube – a symptom of the underlying $k-\epsilon$ models. The hybrid wall treatment, because it is simple to implement, computationally efficient, and easily extensible to $k-\epsilon$ variants without re-calibration, provides a a good alternative to low-Re approaches.

5. Acknowledgments

The author would like to acknowledge Mizanur Rahman for his help in understanding of the compound wall treatment for the $k-\epsilon$ models, and Alvaro Coutinho for his helpful suggestions regarding alternative wall treatments and his early revie of the paper.

References

[1] M. Popovac and K. Hanjalic. Compound wall treatment for RANS computation of complex turbulent flows and heat transfer. *Flow Turbulence and Combustion*, 78:177–202, 2007.

[2] M. M. Rahman and T. Siikonen. Compound wall treatment with low-Re turbulence model. *International Journal for Numerical Methods in Fluids*, 68:706–723, 2012.

[3] S. Saric, B. Basara, and Z. Zunic. Advanced near-wall modeling for engine heat transfer. *International Journal of Heat and Fluid Flow*, 2016. in press – online only.

[4] J. Bredberg. On the Wall Boundary Condition for Turbulence Models. Technical Report 00/4, Chalmers University of Technology, 2000.

[5] X. Albets-Chico, C.D. Perez-Segarra, A. Oliva, and J. Bredberg. Analysis of wall-function approaches using two-equation turbulence models. *International Journal of Heat and Mass Transfer*, 51(19-20):4940–4957, 2008.

[6] P. A. Durbin. Limiters and wall treatments in applied turbulence modeling. *Fluid Dynamics Research*, 41:1–18, 2009.

[7] B. E. Launder and D. B. Spalding. The numerical computation of turbulent flows. *Computer Methods in Applied Mechanics and Engineering*, 3:269–289, 1974.

[8] V. C. Patel, W. Rodi, and G. Scheurer. Turbulence models for near-wall and low Reynolds number flows: a review. *AIAA Journal*, 23(9):1308–1319, 1984.

[9] U. Goldberg, O. Peroomian, and S. Chakravarthy. A wall-distance-free $k-\epsilon$ model with enhanced near-wall treatment. *Journal of Fluids Engineering*, 120:457–462, 1998.

[10] M. M. Rahman and T. Siikonen. A new time scale based low-Re $k-\epsilon$ model. In *3rd International Conference on Computational Heat and Mass Transfer*, 2003.

[11] H. C. Chen and V. C. Patel. Near-wall turbulence models for complex flows including separation. *AIAA Journal*, 26(6):641–648, 1988.

[12] M. Wolfshtein. The velocity and temperature distribution in one-dimensional flow with turbulence augmentation and pressure gradient. *International Journal of Heat and Mass Transfer*, 12:301–318, 1969.

[13] H. Grotjans and F.R. Menter. Wall functions for general application CFD codes. In *ECCOMAS 98 Proceedings of the Fourth European Computational Fluid Dynamics Conference*, pages 1112–1117. John Wiley and Sons, 1998.

[14] T.J. Craft, A.V. Gerasimov, H. Iacovides, and B.E. Launder. Progress in the generalization of wall-function treatments. *International Journal of Heat and Fluid Flow*, 23(2):148–160, 2002.

[15] T.J. Craft, S.E. Gant, A.V. Gerasimov, H. Iacovides, and B.E. Launder. Development and application of wall-function treatments for turbulent forced and mixed convection flows. *Fluid Dynamics Research*, 38(2-3):127–144, 2006.

[16] T.-H. Shih, L. A. Povinelli, and N.-S. Liu. Application of generalized wall function for complex turbulent flows. *Journal of Turbulence*, 4:2–15, 2003.

[17] S. V. Utyuzhnikov. Some new approaches to building and implementing wwall-function for modeling of near-wall turbulent flows. *Computers & Fluids*, 34:771–784, 2005.

[18] Y. Bazilevs, C. Michler, V. M. Calo, and T. J. R. Hughes. Weak Dirichlet boundary condtiions for wall-bounded turbulent flows. *Computer Methods in Applied Mechanics and Engineering*, 196:4853 – 4862, 2007.

[19] Benjamin Krank and Wolfgang A. Wall. A new approach to wall modeling in LES of incompressible flow via function enrichment. *Journal of Computational Physics*, 316:94 – 116, 2016.

[20] T. Knopp, T. Altrutz, and D. Schwamborn. A grid and flow adaptive wall-function method for RANS turbulence modelling. *Journal of Computational Physics*, 220:19–40, 2006.

[21] K. Hajalic, M. Popovac, and M. Hadziabdic. A robust near-wall elliptic-relaxation eddy-viscosity turbulence model for CFD. *International Journal of Heat and Fluid Flow*, 24:1047–1051, 2004.

[22] B. A. Kader. Temperature and concentration profiles in fully turbulent boundary layers. *International Journal of Heat and Mass Transfer*, 81(9):1541–1544, 1981.

[23] P. M. Gresho and R. L. Sani. *Incompressible flow and the finite element method, Advection-diffusion and isothermal laminar flow.* John Wiley & Sons, Chicester, England, 1998.

[24] M. A. Christon, J. Bakosi, B. T. Nadiga, M. Berndt amd M. M. Francois, A. K. Stagg, Y. Xia, and H. Luo. A hybrid incremental projection method for thermal-hydraulics applications. *Journal of Computational Physics*, 317:382 – 404, 2016.

[25] V. Yakhot, S. A. Orszag, S. Thangam, T. B. Gatski, and C. G. Speziale. Development of turbulence models for shear flows by a double expansion technique. *Physics of Fluids*, 4(7):1510–1520, 1992.

[26] Computational Sciences International. The hydra toolkit computatonal fluid dynamics theory manual. Technical Report CSI-2015-1, Computational Sciences International, 2015.

[27] T. Jongen. *Simulation and modeling of turbulent incompressible flows.* PhD thesis, EPF Lausanne, Lausanne, Switzerland, 1992.

[28] H. Riechardt. Vollstandige dartelling der turbulente geschwindigkeitsverteilung in glattne leitungen. *Journal of Applied Mathematics and Mechanics (ZAMM)*, 31(7):208–219, 1951.

[29] R. D. R. D. Moser. Kim and N. N. Mansour. DNS of a turbulent channel flow up to $re_\tau = 590$. *Physics of Fluids*, 11:943 – 945, 1998.

[30] P. R. Spalart and S. R. Allmaras. A one-equation turbulence model for aerodynamic flows. In *AIAA-92-0439*, Reno, Nevada, January 1992. AIAA 30th Aerospace Science Meeting and Exhibit.

[31] E. R. Meinders and K. HanK. Hanjalic. J. Martinuzzi. Experimental study of the local convection heat transfer from a wall-lounted cube in turbulent channel flow. *Transactions of the ASME*, 121:564–573, 1999.

[32] A. Yakhot, H. Liu, and N. Nikitin. Turbulent flow around a wall-mounted cube: A direct numerical simulation. *International Journal of Heat and Fluid Flow*, 27:994–1009, 2006.

[33] Frank M. White. *Viscous Fluid Flow.* McGraw-Hill, Inc., 1974.